Received 7 November 2021; revised 6 March 2022; accepted 31 March 2022. Date of publication 6 April 2022; date of current version 16 June 2022.
The review of this article was arranged by Editor P. Pavan.

Digital Object Identifier 10.1109/JEDS.2022.3165315

Solution-Processed Small Molecule Inverted Solar Cells: Impact of Electron Transport Layers

MAGALY RAMÍREZ-COMO [1] (Member, IEEE), VICTOR S. BALDERRAMA [2] (Member, IEEE), JOSÉ G. SÁNCHEZ [3] (Member, IEEE), ANGEL SACRAMENTO [4] (Member, IEEE), MAGALI ESTRADA [4] (Senior Member, IEEE), JOSEP PALLARÈS [1] (Senior Member, IEEE), AND LLUIS F. MARSAL [1] (Senior Member, IEEE)

1 Departament d'Enginyeria Electronica Electrica i Automatica, Rovira i Virgili University, 43007 Tarragona, Spain
2 CONACYT—Center for Engineering and Industrial Development (CIDESI), Microtechnology Division (DMT), Santiago de Querétaro, Querétaro 76125, Mexico
3 Institute of Chemical Research of Catalonia, The Barcelona Institute of Science and Technology, 43007 Tarragona, Spain
4 Sección de Electrónica del Estado Sólido, Departamento de Ingeniería Eléctrica, CINVESTAV-IPN, Mexico City 07360, Mexico

CORRESPONDING AUTHOR: L. F. MARSAL (e-mail: lluis.marsal@urv.cat)

This work was supported in part by the Diputació de Tarragona under Grant 2021CM14; in part by the Spanish Ministry of Science and Innovation (MICINN/FEDER) under Grant RTI2018-094040-B-I00; in part by the Agency for Management of University and Research Grants (AGAUR) under Grant 2017-SGR-1527; in part by the ICREA under the ICREA Academia Award; and in part by the SEP-CINVESTAV in Mexico under Project 32. The work of Victor S. Balderrama was supported by the Cátedras CONACYT para Jóvenes Investigadores under Project 2, through Project "Laboratorio Nacional SEDEAM CONACYT" under Grant 314841, and through Project FORDECYT under Grant 297497. The work of Angel Sacramento was supported by the CONACYT for Ph.D. Scholarships 295606.

ABSTRACT In this work, the use of poly [(9,9-bis (30- (N,N-dimethylamino) propyl) -2,7-fluorene) -alt-2,7- (9,9-dioctylfluorene) (PFN) as electron transport layer (ETL) in inverted small molecule solar cells (SM-iOSCs) is analyzed. The optical and electrical characteristics obtained are compared with those obtained for similar SM-iOSCs where the ETL was zinc oxide. The p-DTS$(FBTTh_2)_2$ and $PC_{70}BM$ materials are used as donor and acceptor in the bulk heterojunction active layer, respectively for all devices. The photovoltaic devices exhibited a power conversion efficiency of 6.75% under 1 sun illumination. Impedance measurements were used to understand the causes that dominate the performance of the devices. We found that the loss resistance is governed by the PFN layer, which results in a lower fill factor value. Studies of atomic force microscopy, external quantum efficiency, and absorption UV-vis on the active layer have been performed to understand the effects of the charge transport dynamics on the performance of the devices.

INDEX TERMS Buffer layers, dependence light intensity, electron transport layer, impedance spectroscopy, organic solar cells, p-DTS$(FBTTh_2)_2$:$PC_{70}BM$ solar cells, PFN ETL, Solution-processed small molecule, ZnO ETL.

I. INTRODUCTION

During the last years, organic solar cells (OSCs) have increased their the power conversion efficiency (PCE) rapidly due to the development of new organic semiconductor materials, such as small molecule, which have improved charge carrier mobility and light absorption [1]–[3]. From the point of view of cell structures, inverted organic solar cells (iOSCs) have shown to be the best alternative to OSC on issues of degradation and stability in comparison with organic solar cells conventional [4], [5].

Several buffer layers combined with a low work function metal electrodes have been reported to improve the performance and lifetime of organic solar cells. In iOSCs, as hole transport layer (HTL) are used commonly vanadium oxide (V_2O_5) [6], [7], molybdenum oxide (MoO_3) [8], [9] and nickel oxide (NiO) [10], [11]. As electron transport layer (ETL) are used commonly PFN [12], [13], zinc oxide (ZnO) [14], [15] and titanium oxide (TiO_x) [16], [17]. In order to achieve high-performance devices, the ETLs must possess low light absorption to ensure a better charge generation in the active layer, and have a good band matching to the active layer to improve both the electron collection and hole blocking [18].

On the other hand, iOSCs based on small molecule donor:fullerene active layer (SM-iOSCs) have achieved high efficiencies, up to 11% [19], [20]. Compared to polymers, small molecules or oligomers, as donor materials, have advantages such as relatively simpler synthesis, well-defined chemical structure, and reduced molecular weight variations from batch to batch [21], [22]. Moreover, the energy levels of the small molecule material can be relatively easily tuned by slightly modifying their chemical structures [23]. Also, SM-OSCs can have tuned optical band gaps, providing an absorption spectrum that matches with emission spectra of several indoor lights, e.g., LED, FLs (fluorescent lamp), and halogen lights, which have different emitting spectra.

In this paper, we study the performance of an inverted bulk-heterojunction (BHJ) SM-iOSC using PFN as ETL. Devices were fabricated using 7,7′-(4,4-bis (2-ethylhexyl)-4H-silolo[3, 2-b:4, 5-b′]dithiophene-2, 6-diyl) bis(6 - fluoro - 4 - (5′ - hexyl-[2,2′ - bithiophen]-5 - yl)benzo[c] [1,2,5] thiadiazole) (p-DTS($FBTTh_2$)$_2$) as donor material and [6-6]-phenyl C_{70} butyric acid methyl ester ($PC_{70}BM$) as acceptor material. The fabricated device structure is ITO/PFN/p-DTS($FBTTh_2$)$_2$:$PC_{70}BM$/V_2O_5/Ag. We compare these devices with another control reference structure, which uses ZnO as ETL. Therefore, two types of structures have been studied with different ETL: PFN (type I), and as control reference structure ZnO (type II). The current density–voltage (J–V) curves were measured for both groups of SM-iOSCs under dark and under illumination using AM 1.5 G spectrum to one sun to extract the performance parameters. Impedance spectra have been also measured under light at different bias voltages. The results are fitted to a circuit model consisting of three RC elements in series. Each of the RC elements is associated with one of the layers forming the solar cell. The extracted circuital parameters are related to the transport processes occurring in the cell. Optical and morphological properties of the devices, such as absorbance, incident quantum external efficiency (EQE), and atomic force microscope (AFM) characterization, were obtained to understand that factors limit the PCE.

II. EXPERIMENTAL DETAILS

A. MATERIALS

ITO-coated glass substrates (with a nominal sheet resistance of 10 Ω/square and 220 nm of thickness) were purchased from PsiOTec Ltd. p-DTS($FBTTh_2$)$_2$ and PFN materials were purchased from One-material Company. The $PC_{70}BM$ was purchased from Solenne BV. The V_2O_5 (99.9%) and zinc acetate dihydrate were purchased from Sigma-Aldrich. High-purity silver (99.99%) wire was obtained from Testbourne Ltd.

B. PREPARATION OF PRECURSOR SOLUTIONS ETL

The PFN material was dissolved in methanol to a concentration of 1.84 mg/ml, using acetic acid (1.84 μl/mL) as additive. The solution was left under stirring for 18 h at 40 °C. The ZnO precursor was prepared by dissolving zinc acetate dihydrate 0.68 M and ethanolamine 0.46 M in 2-methoxyethanol leaving the solution under vigorous stirring for 1 h at 70 °C. Subsequently, the precursor solution of ZnO was diluted in methanol in a 1:1 ratio.

C. SOLAR CELLS FABRICATION

Inverted devices were based on the structure of ITO/ETL/p-DTS($FBTTh_2$)$_2$:$PC_{70}BM$/V_2O_5/Ag. PFN or ZnO was used as ETL and spin-coated on the pre-cleaned patterned ITO glass substrates. PFN was deposited at 4200 rpm for 60 s, obtaining a thickness of 10 nm. ZnO was deposited for 30 s at 3000 rpm. The resulting ZnO film was heated at 110 °C for 1 h in air, obtaining a thickness of 30 nm. The process of preparing the p-DTS($FBTTh_2$)$_2$:$PC_{70}BM$ solution is carried out as detailed in [24], [25]. Using spin coating, the active layer was deposited on top of the ETL, varying the spinning speed from 900 to 1300 rpm, for 45 s. The obtained thicknesses were from 210 to 90 nm. The obtained films were annealed at 75 °C, for 15 min, to evaporate the residual solvent. Finally, the anode layer was deposited consisting of 5 nm of V_2O_5 followed by 100 nm of Ag, were deposited by thermal evaporation at 1×10^{-6} mbar. The active area of the device was 0.09 cm^2.

D. SOLAR CELLS CHARACTERIZATION

All the J–V characteristics of the devices under light and dark were performed at room temperature, using a solar simulator (Abet Technologies model 11 000 class type A, Xenon arc) under AM 1.5G spectrum and a Keithley 2400 Source-Measure Unit. The light intensity was calibrated with an NREL certified monocrystalline silicon photodiode until it reached 1 sun of intensity. To achieve different light intensities, under one sun illumination, a series of optical density filters were employed. The EQE spectra of the solar cells were measured using Lasing IPCE-DC model equipment. The system was calibrated using a photodiode in the device under test position. The optical absorption was measured at room temperature from 300 nm to 800 nm, using a Perkin Elmer UV-Visible-NIR Lambda 950 spectrophotometer with an integrating sphere. The AFM topography of the samples was obtained in tapping mode on a molecular imaging model pico SPM II (pico+). Images were recorded under air using silicon probes with a typical spring constant of 1–5 $nN{\cdot}m^{-1}$ and a resonant frequency at 75 kHz. Impedance spectroscopy (IS) was carried out in the frequency range between 10 Hz and 2 MHz, using an Agilent E4980A LCR meter. Several voltage perturbations (0, 0.25, 0.50, 0.79 and 1 V) were applied with an AC signal and 20 mV amplitude. During the measurements, the devices were exposed to 1 sun under AM1.5G spectrum illumination.

III. RESULTS AND DISCUSSION

We analyzed two structures, which we referred to as:

Type I - ITO/PFN/p-DTS($FBTTh_2$)$_2$:$PC_{70}BM$/V_2O_5/Ag

Type II - ITO/ZnO/p-DTS($FBTTh_2$)$_2$:$PC_{70}BM$/V_2O_5/Ag

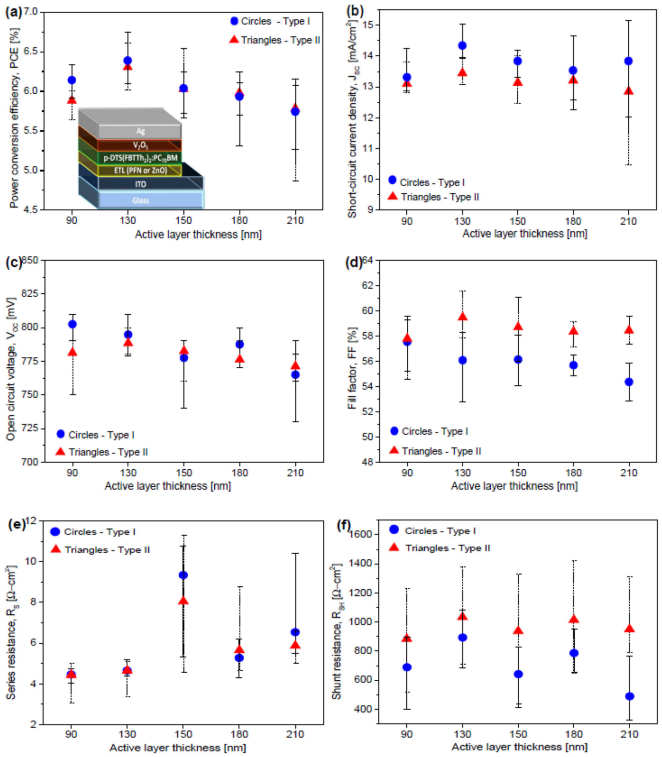

FIGURE 1. The active layer thickness dependent performance parameters for cells type I and II: (a) PCE; (b) J_{SC}; (c) V_{OC}; (d) FF; (e) R_S and (f) R_{SH}. Error bars correspond to the maximum and minimum obtained for the respective condition. Inset (a) the device structure of the BHJ-iOSCs with p-DTS(FBTTh$_2$)$_2$:PC$_{70}$BM as the active layer.

The performance of these SM-iOSCs, under AM 1.5G spectrum at one sun condition (100 mW/cm^2), was first studied. To optimize the thickness of the p-DTS(FBTTh$_2$)$_2$:PC$_{70}$BM layer, five different thicknesses from 90 nm to 210 nm were deposited. Inset Fig. 1(a) shows the schematic representation of the fabricated SM-iOSCs. The performance parameters PCE, short-circuit current density (J_{SC}), open circuit voltage (V_{OC}), fill factor (FF), series and shunt resistances (R_S and R_{SH}) of the SM-iOSCs are shown in Fig. 1 for the different p-DTS(FBTTh$_2$)$_2$:PC$_{70}$BM layer thicknesses. The best average performance for both types of devices was observed for an active layer thickness of 130 nm, obtaining an average PCE of 6.39% for type I and 6.31%. for type II. Fig. 2(a) shows the current density vs. voltage (J-V) characteristics for the best device with 130 nm. The highest PCE value obtained for type I cells was 6.75%, for an active layer thickness of 130 nm, using PFN as ETL in an inverted structure. In type II cells, the highest PCE was 6.61%, also for 130 nm thickness. These values agree well with published results for inverted organic solar cells based in similar stacks using ZnO as ETL [26], [27].

From Fig. 1 is observed that the thickness of 130 nm was the optimum from the point of view of the parameters PCE, J_{SC}, and V_{OC}. The maximum value of V_{OC} obtained was 0.81 V, very close to the theoretical value of 0.82 V, given by the difference between the HOMO level of the donor p-DTS(FBTTh$_2$)$_2$ of −5.12 eV and the LUMO level of the PC$_{70}$BM acceptor of −4.3 eV [7], [18], [28].

In Fig. 1(e) is observed that the average value R_S of these SM-iOSCs is higher than 4 Ω-cm^2, comparing it with polymer solar cells (PSC) whose value is around 1.5 Ω-cm^2 [17], [24]. A higher value of R_S is a possible cause of the lower value of the J_{SC}, as well as the FF and PCE of the SM-iOSCs. However, when these parameters were analyzed based on the thickness of the active layer, no correlation was found with the behavior of the R_S, which did not show a defined trend. The R_{SH} also did not show a definite trend.

The EQE of the SM-iOSCs is shown in Fig. 2(b). The EQE spectrum of the SM-iOSCs with higher values is for the thickness of 130 nm of the type I structure (blue line). For this same thickness, the EQE spectrum values were lower for the type II devices (red line). This qualitatively justifies the decrease in J_{SC} observed in Fig. 1(b) for type II cells concerning type I cells. The EQE depends on the absorption efficiency. Therefore, it depends on the absorption spectrum of the ETL because the light across this layer to be absorbed for the active layer. If the ETL has an increase in absorption in some regions of the electromagnetic spectrum, then fewer photons will pass through it and lead to a reduction in the absorption by the active layer. In figure 2(c) it is observed that the PFN layer has an increase in absorption around 400 nm while ZnO does not present this increase. For the above, it is observed that both devices, exhibit a slightly different spectral shape from 300 nm to 450 nm in the EQE spectrum. The J_{SC} values obtained by integrating the EQE with the reference spectrum AM 1.5G, are shown inset Fig. 2(b). These values corroborate the trend previously observed for the J_{SC} concerning the thickness of the type I devices. A similar situation occurs in the type II devices (not shown). The J_{SC} values obtained for the 130 nm devices were 14.40 mA/cm^2 and 13.27 mA/cm^2 for structure type I and type II, respectively, which agree well with the J_{SC} value obtained from the J-V characteristics.

Fig. 2(c) shows the absorption spectra of the ETL and ETL/p-DTS(FBTTh$_2$)$_2$:PC$_{70}$BM deposited on the ITO substrate for both types of devices obtained from UV-Vis spectroscopy analysis. It is well known that the absorption spectrum of ITO shows a peak centered around 480 nm [2], [29]. The absorption spectrum for PFN (purple line) shows a shoulder at 400 nm and the absorption peak originating from ITO centered at 480 nm. For the ZnO layer (orange line), the absorption spectrum shows the redshift of the ITO absorption peak from 480 nm to 516 nm. The shift of the ITO peak is due to the absorption of the material deposited on the ITO layer. The absorbance region in the 350 nm to 800 nm wavelength range is nearly transparent to the two ETLs, allowing most of the photons to be absorbed by the active layer. The ETL/p-DTS(FBTTh$_2$)$_2$:PC$_{70}$BM absorption spectra were observed for the different active layer thicknesses corresponding to type I devices in Fig. 2(c). The absorption spectrum of the donor layer corresponding to

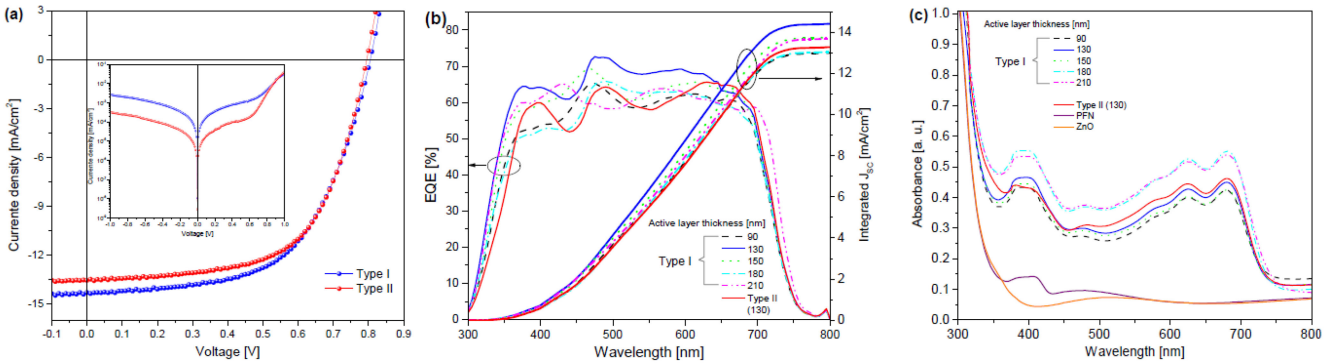

FIGURE 2. ***J-V*** **characteristics of the p-DTS(FBTTh$_2$)$_2$:PC$_{70}$BM BHJ solar cells with PFN (type I) and ZnO (type II) as ETL (130 nm thickness), measured under 100 mW/cm^2 AM 1.5G irradiation. Inset (a)** ***J-V*** **characteristics of type I and II cells under dark. (b) EQE spectra of type I cells with different thicknesses and type II cells with 130 nm. Inset (b) show the integrated J_{SC} of type I and II devices. (c) UV-vis optical absorption spectra of the films PFN/p-DTS(FBTTh$_2$)$_2$:PC$_{70}$BM (type I at different thicknesses), ZnO/p-DTS(FBTTh$_2$)$_2$:PC$_{70}$BM (Type II at 130 nm thickness, red line), PFN (purple) and ZnO (orange). All deposited on glass/ITO under fabrication conditions similar to those used to fabricate the cells.**

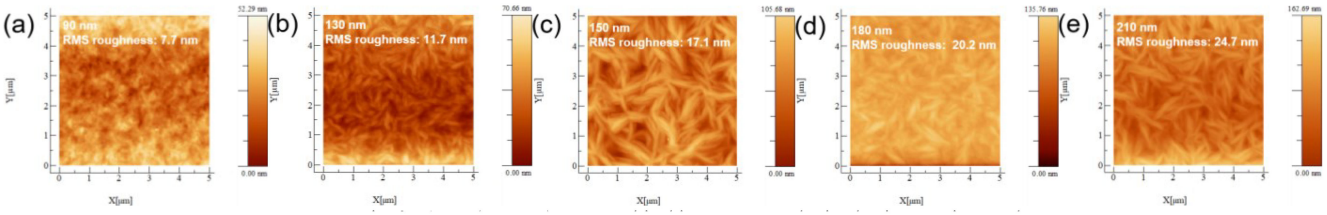

FIGURE 3. **AFM (5×5 μm) topographical images were obtained using tapping mode.**

the small molecule p-DTS(FBTTh$_2$)$_2$, presents three maximum absorption peaks located around 400 nm, 625 nm, and 680 nm [30]–[32]. In both types of devices, the last two peaks of 625 nm and 680 nm can be appreciated, which is attributed to a vibronic structure of p-DTS(FBTTh$_2$)$_2$, since these peaks correspond to vibronic transitions 0-1 and 0-0, respectively [33]. The absorption peak at 680 nm could be attributed to the π-π stacking and molecular interaction inside the p-DTS(FBTTh$_2$)$_2$ phase [27], [34]. Regarding the peak at 400 nm referred to the p-DTS(FBTTh$_2$)$_2$ molecule, it can be seen that the type II device (red line) exhibits it slightly, and also another peak is observed at 375 nm, which belongs to the acceptor material, the fullerene PC$_{70}$BM, as well as the peak at 480 nm [35]–[37]. However, in the type I device the first two peaks (375 nm and 400 nm) do not differ. Instead, a maximum width is observed. This is due to the absorption of the PFN layer, which has a shoulder at 400 nm, an absorption that is not found in the ZnO layer.

With respect to the dependence of the thickness of the active layer, Fig. 2(c) shows that thicker layers absorb more than thinner ones. However, higher absorption did not mean higher efficiency as seen in Fig. 1(a). It is well known that the J_{SC} is determined by the product of the density of photoinduced charge carriers and the mobility of the charge carrier [38]. As well as the EQE considers the absorption efficiency and the separation, transport, and collection of charge within the cells. Then, if type I and type II devices have a low EQE spectrum (Fig. 2(b)) and a high absorption (Fig. 2(c)), it can be concluded that charge transport is the limiting factor for the performance of these SM-iOSCs.

In order to evaluate the evolution of the morphology of the surface of the active layer concerning the variation of its thickness and to understand the relationship between the morphology and the performance of the SM-iOSCs, the morphology of the active layer was investigated through AFM. All the films were deposited in identical conditions as were fabricated the solar cells. Fig. 3 shows the topography of the active layer with thicknesses from 90 nm to 210 nm. Layers 130 nm to 210 nm thickness, (Fig. 3(b)-(e)), show domains like fibers or grains of rice with widths ranging from 30-90 nm and lengths from 200-700 nm. In the micrographs, it is evident that the size of the domains tends to increase as the thickness increases. These domains should be attributed to regions of p-DTS(FBTTh$_2$)$_2$ within the active layer rather than PC$_{70}$BM [39]. It has been shown by Zhang *et al.* that the presence of these domains in the film is attributed to the p-DTS(FBTTh$_2$)$_2$ and the heat treatment causes the aggregates to become larger [40]. Together, the fact that the active layer solution contains a small amount of diodoctane as an additive promotes the formation of these fibers, which are interconnected networks of domains of p-DTS(FBTTh$_2$)$_2$, as has been seen in other studies [41]–[43]. Furthermore, the observed domains of p-DTS(FBTTh$_2$)$_2$ in the film of the mixture are consistent with the observed absorption peaks corresponding to the vibronic structure of p-DTS(FBTTh$_2$)$_2$ in the UV-Vis absorption spectra indicating the presence of these domains [31], [34].

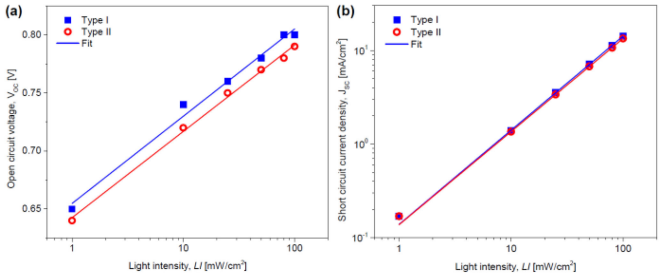

FIGURE 4. (a) V_{OC} as a function of light intensity for type I and type II cells. The curves were fitted (lines) using (2). (b) J_{SC} as a function of light intensity of type I and type II cells. The curves were fitted (lines) in the form of (3).

The root-mean-square (RMS) surface roughness obtained from the AFM height profiles in a measurement area of 25 μm^2 ranged from 7.7 nm to 24.7 nm, showing a linear dependence with the active layer thickness. This increase in the RMS values of the films is related to the increase in the size of the domains. The surface roughness and the size of the domain increase slightly as the thickness of the sample increases. We can say that the fact that the roughness will increase may suggest that it directly influenced the performance of type I and type II cells. It was observed that the higher the roughness, the lower the average PCE (Fig. 1(a)). It is suggested that the high value of the roughness obtained, and the large domain size is likely to be one of the causes of the low J_{SC} observed for both groups of SM-iOSCs, since the large domain sizes lead to excitons in the active layer, they may not be able to reach the donor/acceptor interface, and subsequently dissociate into free carriers. This is reflected in the J_{SC}, in addition to that it depends directly on the mobility of the carrier, which in turn is sensitive to the morphology of the thin film of organic semiconductors [38]. Therefore, the observed variation of the J_{SC}, the increase in the roughness and size of domains concerning the active layer thickness shows that both the mobility and the exciton dissociation ratio are decreasing with increasing active layer thickness. That is, the charge transport process is the main factor that is being affected by the thickness. Xu *et al.* observed that the increase in roughness in the p-DTS(FBTTh$_2$)$_2$:PC$_{70}$BM layer implies effects on charge transport and degrades the mobility of holes and electrons [31]. Therefore, this leads us to conclude that the J_{SC} decreases more due to the effect of charge transport than due to resistance.

To obtain information about how the ETL and active layer morphology affect transport mechanisms within the active layer of devices is to calculate their ideality factor (n_{id}). The J-V characteristics of the best devices with thicknesses of 130 nm were obtained for type I and type II devices and illuminated at different light intensities (*LI*) under the AM 1.5G spectrum. Fig. 4(a) shows the dependence of V_{OC} on the logarithm of the *LI*. This dependency describes the order of the recombination processes in the BHJ film [44]. Equation (1) predicts the behavior of the slope *kT/q* of the V_{OC} versus the natural logarithm of the *LI*, which has been experimentally observed in several works [45]–[47] and is commonly expressed as:

$$V_{oc} = n_{id}\left(\frac{kT}{q}\right) \ln\ (LI) + cte \tag{1}$$

Therefore, the value of n_{id} will also indicate the dominant recombination mechanism in the cell. The slope of V_{OC} versus ln (*LI*) is known to approach *kT/q* when Langevin recombination is dominant. On the other hand, a slope greater than *kT/q* is expected for trap-assisted recombination, i.e., a stronger dependence on light intensity [48]. The value of n_{id} was obtained from the V_{OC} vs. ln (*LI*) graph using (2). The n_{id} value for both type I and type II devices lie within the range of expected values ($1 < n_{id} < 2$) for OSC. These values were 1.26 and 1.25 for type I and type II devices, respectively. For this reason, the transport mechanism seems to be a combination of diffusion and recombination. It is observed that the n_{id} value for SM-iOSC is greater than 1.2, which indicates, in accordance with the aforementioned, that Langevin-type recombination is not the one that is dominating in these devices. There is another type of recombination called Shockley-Read-Hall (SRH), which involves trap-assisted recombination. Therefore, it is suggested that in SM-iOSC there is also this type of recombination.

Figure 4(b) shows the plot of J_{SC} vs. *LI* on a log-log scale. A power-law dependence of J_{SC} under illumination intensity is generally observed in OSC and can be expressed as:

$$J_{SC} \propto\ (LI)^b \tag{2}$$

where *LI* is the intensity of the light and *b* is the exponential factor [40]. The graph of Fig. 4(b) was fitted by a power-law using (3). The *b* value was 1.00 and 0.99 for the devices with structure type I and type II, respectively. The obtained indicates that the majority of free charge carriers are collected on the electrodes before recombination, i.e., non-geminated recombination is not significant in this type of iOSCs [49].

To further analyze the charge transport properties of the layers that make up the solar cell, impedance spectroscopy (IS) measurements were performed on both devices. Figures 5(a) and (b) show the impedance spectra measured under the AM 1.5G spectrum at different voltages for both device types (130 nm). The Nyquist plots of both devices resemble a depressed semicircle for all applied voltages, which is classic behavior of BHJ solar cells, attributed to the generation and recombination of charge carriers and charge transport [43]. The experimental impedance spectra were fitted using an electrical model with three resistor/capacitor (RC) circuits in series and each element of the equivalent circuit is associated with the resistance and capacitance one layer of the iOSCs [44], [50] (see Fig. 5(h)). In our case, we related capacitance C_1 to the ETL (PFN or ZnO), C_2 to the bulk (active layer), and C_3 to the V_2O_5. Since C_1, C_2, and C_3 are the components of the RC circuits,

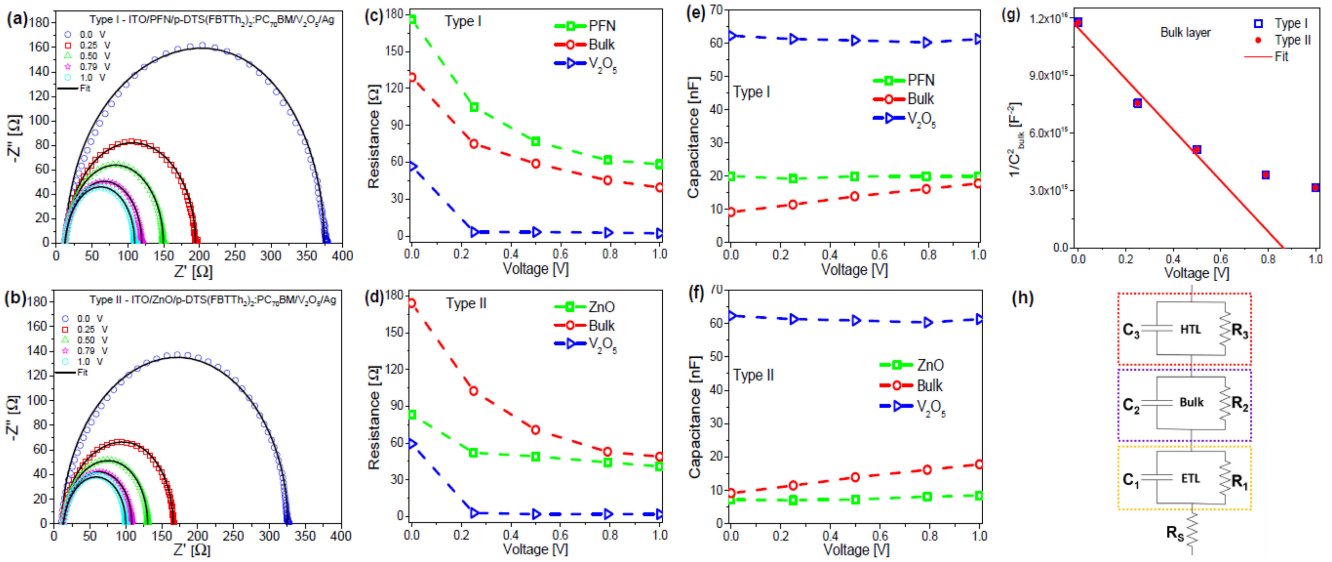

FIGURE 5. **(Open symbols) Experimental impedance spectra response for (a) type I and (b) type II structure, measured under 1 sun conditions at several applied voltages: 0, 0.25, 0.5, 0.79 and 1 V. Resistance R_1, R_2 and R_3, extracted from fits for the type I and type II structure are shown in (c) and (d), respectively. Capacitance C_1, C_2, and C_3, extracted from fits for the type I and type II structure are shown in (e) and (f), respectively. (g) shows $1/C^2$ vs V resembling typical Mott-Schottky behavior. Solid lines in (a) and (b) show the modeled impedance, using the three RC circuit model shown in (h).**

TABLE 1. **Relative dielectric permittivity, thickness and capacitance for each layer.**

Layer	Permittivity [F/m]	Thickness [nm]	Capacitance [nF]
PFN	3.5	10	26.4
ZnO	4.0	30	10.6
p-DTS(FBTTh$_2$)$_2$:PC$_{70}$BM	5.3	130	3.3
V_2O_5	5.0	5	75.4

the three associated resistances were related to each layer. An additional series resistor (R_S) is needed to model ohmic contact resistance and wire effects, which is largely related to substrate resistance. We found that the fitted value for R_S varies from 8Ω to 12Ω, which falls in the range of the ITO sheet resistance value (approximately 10 Ω/sq).

The geometric capacitance of each layer can be theoretically calculated as $C_g = \varepsilon\varepsilon_0 A/L$, where ε_0 is the vacuum dielectric permittivity, ε is the relative dielectric permittivity for the layer, A is the device area and L is the layer thickness. Table 1 shows the calculated capacitance values for each layer in the structure [51]–[54]. These values were used to begin the fitting, which was performed in IviumSoft software. The fitting by optimization obtained using the model of the three RC circuits, at different voltages and for over the whole frequency range is shown in Fig. 5(a) and (b).

Fig. 5(c) and (d) show the resistance and Fig. 5(e) and (f) capacitance values extracted from the three RC circuital model. The resistance of ETL (PFN or ZnO), the active layer and the V_2O_5 layer decreases as the applied voltage increases, in both devices. For type I devices, the highest resistance value is for the PFN layer, which decreases from $\sim$ 180Ω at 0 V to $\sim$ 60Ω at 1 V. These high resistance values at low voltages (0 V to 0.25 V) suggest that for devices I, the shunt resistance (R_{SH}) is mainly determined by the PFN layer. On the other hand, for type II devices, the active layer is the one that shows the highest resistance values, decreasing from $\sim$ 180Ω at 0 V to $\sim$ 50Ω at 1 V, suggesting that, in type II devices, the active layer is dominating the observed value of the shunt resistance. In other words, it can be said that the layer responsible for achieving greater PCE in the type I devices is that of PFN. However, for the type II structure, the active layer dominates its performance.

From Fig. 5(e) and (f) we noticed three regions for capacitance values separated. The capacitance values of ETL (PFN or ZnO) and V_2O_5 remain practically constant, however, the capacitance for the bulk layer rises as the applied voltage increases for both devices. The capacitance of the active layer extracted from the fit is attributed to the depletion region due to the band bending at the contact [55]. In Fig. 5(g) we observe that the capacitance of the bulk layer exhibits a voltage dependence according to the Mott-Schottky relation [56]:

$$\frac{1}{c^2} = \frac{2}{A^2 q\varepsilon\varepsilon_n N_A}(V_{bi} - V) \tag{3}$$

where V_{bi} is the built-in voltage, V is the applied voltage, N_A is the concentration of acceptor impurities, and q accounts for the elementary charge. Fig. 5(g) shows the fit of the capacitance using (4), which exhibits a straight line over a voltage range from 0 V to 0.5 V, leading $V_{bi} = 0.86$ V. Our fits are made in measurements under AM 1.5G illumination, obtaining a concentration of carriers under these conditions of $2.76\times10^{17}\text{cm}^{-3}$. Other authors report the acceptor density of $4.1\times10^{16}\text{cm}^{-3}$ using IS under darkness [53].

IV. CONCLUSION

In summary, is reported an inverted structure SM BHJ solar cell using PFN as electron transport layer with a maximum power conversion efficiency (PCE) under AM 1.5 G spectrum (1 sun) of 6.75%, which is among one of the higher values for inverted structure small-molecule solar cells based in p-DTS(FBTTh$_2$)$_2$ reported to date. The highest PCE was obtained for a thickness of 130 nm of p-DTS(FBTTh$_2$)$_2$:PC$_{70}$BM. Theses structure is compared to similar cells with ZnO as ETL. The analysis of the UV-Vis absorption and EQE spectra was possible to determine that charge transport is the limiting factor in the performance of SM-iOSCs. The value extracted from the ideality factor showed that the transport mechanism is a combination of diffusion and recombination. Furthermore, from the dependence of J_{SC} with the light intensity, it was obtained that the non-geminated recombination is not significant, that is to say, most free charge carriers are efficiently collected at the electrodes. The images of the morphology and measurements of the roughness made through AFM gave a guideline to indicate that the high value of roughness (7.7 nm to 24.7 nm) and the large domain size (widths of 30-90 nm) of the active layer of the SM-iOSCs are one of the causes of the low value of J_{SC} observed for these devices, since the large domain sizes mean that the excitons in the active layer may not be able to reach the donor/acceptor interface, to dissociate into free charge carriers. Finally, using impedance spectroscopy, we show that the PFN layer (ETL) has a greater influence on the value that the shunt resistance takes in SM-iOSCs.

REFERENCES

[1] A. A. A. Torimtubun *et al.*, "Fluorinated Zinc and Copper phthalocyanines as efficient third components in ternary bulk heterojunction solar cells," *ACS Appl. Energy Mater.*, vol. 4, no. 5, pp. 5201–5211, May 2021.

[2] V. S. Balderrama *et al.*, "High-efficiency organic solar cells based on a halide salt and polyfluorene polymer with a high alignment-level of the cathode selective contact," *J. Mater. Chem. A*, vol. 6, no. 45, pp. 22534–22544, 2018.

[3] G. Lastra *et al.*, "High-performance inverted polymer solar cells: Study and analysis of different cathode buffer layers," *IEEE J. Photovolt.*, vol. 8, no. 2, pp. 505–511, Mar. 2018.

[4] A. Sacramento, V. S. Balderrama, M. Ramírez-Como, L. F. Marsal, and M. Estrada, "Degradation study under air environment of inverted polymer solar cells using polyfluorene and halide salt as electron transport layers," *Solar Energy*, vol. 198, pp. 419–426, Mar. 2020.

[5] M. Ramírez-Como, V. S. Balderrama, A. Sacramento, L. F. Marsal, G. Lastra, and M. Estrada, "Fabrication and characterization of inverted organic PTB7:PC$_{70}$BM solar cells using Hf-In-ZnO as electron transport layer," *Solar Energy*, vol. 181, pp. 386–395, Mar. 2019.

[6] G. Lastra *et al.*, "Air environment degradation of a high-performance inverted PTB7-Th:PC70BM solar cell," *IEEE J. Photovolt.*, vol. 9, no. 2, pp. 464–468, Mar. 2019.

[7] M. Ramirez-Como, V. S. Balderrama, and M. Estrada, "Performance parameters degradation of inverted organic solar cells exposed under solar and artificial irradiance, using PTB7:PC$_{70}$BM as active layer," in *Proc. 13th CCE*, 2016, pp. 1–5.

[8] A. Sacramento *et al.*, "Comparative degradation analysis of V_2O_5, MoO_3 and their stacks as hole transport layers in high-efficiency inverted polymer solar cells," *J. Mater. Chem. C*, vol. 9, no. 20, pp. 6518–6527, 2021.

[9] C. Xu *et al.*, "A wide temperature tolerance, solution-processed MoOx interface layer for efficient and stable organic solar cells," *Solar Energy Mater. Solar Cells*, vol. 159, pp. 136–142, Jan. 2017.

[10] A. Sacramento, V. S. Balderrama, M. Ramírez-Como, J. G. Sánchez, M. Estrada, and L. F. Marsal, "Inverted polymer solar cells using V_2O_5/NiO as anode selective contact: Degradation study," in *Proc. IEEE LAEDC*, 2020, pp. 1–4.

[11] W. Yang, Z. Yu, W. Liu, C. Li, and H. Chen, "Aqueous solution-processed NiOx anode buffer layers applicable for polymer solar cells," *J. Polym. Sci. Part A Polym. Chem.*, vol. 55, no. 4, pp. 747–753, Feb. 2017.

[12] L. Reséndiz, V. S. Balderrama, G. Lastra, M. Ramírez, V. Cabrera, and M. Estrada, "Optimization of PFN thickness in inverted high-performance PTB7:PC70BM solar cells," *Solid-State. Electron.*, vol. 153, pp. 33–36, Mar. 2019.

[13] V. S. Balderrama *et al.*, "Organic solar cells toward the fabrication under air environment," *IEEE J. Photovolt.*, vol. 6, no. 2, pp. 491–497, Mar. 2016.

[14] M. Ramirez-Como, A. Sacramento, J. G. Sanchez, L. F. Marsal, V. S. Balderrama, and M. Estrada, "Impact of the hafnium oxide as hole blocking layer on the performance of organic solar cells," in *Proc. IEEE LAEDC*, San José, Costa Rica, 2020, pp. 1–5.

[15] E. Moustafa, J. G. Sánchez, L. F. Marsal, and J. Pallarès, "Stability enhancement of high-performance inverted polymer solar cells using ZnO electron interfacial layer deposited by intermittent spray pyrolysis approach," *ACS Appl. Energy Mater.*, vol. 4, no. 4, pp. 4099–4111, 2021.

[16] A. A. A. Torimtubun, J. G. Sánchez, J. Pallarès, and L. F. Marsal, "A cathode interface engineering approach for the comprehensive study of indoor performance enhancement in organic photovoltaics," *Sustain. Energy Fuels*, vol. 4, no. 7, pp. 3378–3387, 2020.

[17] J. G. Sánchez *et al.*, "Stability study of high efficiency polymer solar cells using TiOxas electron transport layer," *Solar Energy*, vol. 150, pp. 147–155, Jul. 2017.

[18] J. Huang and H. Huang, "Inverted organic solar cells (OSCs)," in *Organic and Hybrid Solar Cells*. Cham, Switzerland: Springer, 2014, pp. 2015–2039.

[19] J. Wan, X. Xu, G. Zhang, Y. Li, K. Feng, and Q. Peng, "Highly efficient halogen-free solvent processed small-molecule organic solar cells enabled by material design and device engineering," *Energy Environ. Sci.*, vol. 10, no. 8, pp. 1739–1745, 2017.

[20] T. Duan *et al.*, "Simple organic donors based on halogenated oligothiophenes for all small molecule solar cells with efficiency over 11%," *J. Mater. Chem. A*, vol. 8, no. 12, pp. 5843–5847, 2020.

[21] K. Cho *et al.*, "Reducing Trap-Assisted Recombination in Small Organic Molecule-Based Photovoltaics by the Addition of a Conjugated Block Copolymer," *Macromol. Rapid Commun.*, vol. 39, no. 5, pp. 1–6, Mar. 2018.

[22] B. Walker, C. Kim, and T.-Q. Nguyen, "Small molecule solution-processed bulk heterojunction solar cells," *Chem. Mater.*, vol. 23, no. 3, pp. 470–482, 2011.

[23] R. B. Zerdan *et al.*, "The influence of solubilizing chain stereochemistry on small molecule photovoltaics," *Adv. Funct. Mater.*, vol. 24, no. 38, pp. 5993–6004, 2014.

[24] M. Ramírez-Como *et al.*, "Small molecule organic solar cells toward improved stability and performance for Indoor Light Harvesting Application," *Solar Energy Mater. Solar Cells*, vol. 230, Jun. 2021, Art. no. 111265.

[25] M. Ramírez-Como, A. Sacramento, J. G. Sánchez, M. Estrada, V. S. Balderrama, and L. F. Marsal, "Impact of hole blocking layer on the performance of solution-processed small molecule solar cells," in *Proc. IEEE LAEDC*, 2021, pp. 1–4.

[26] A. K. K. Kyaw *et al.*, "Efficient solution-processed small-molecule solar cells with inverted structure," *Adv. Mater.*, vol. 25, no. 17, pp. 2397–2402, 2013.

[27] W. Zhou *et al.*, "Surface treatment by binary solvents induces the crystallization of a small molecular donor for enhanced photovoltaic performance," *Phys. Chem. Chem. Phys.*, vol. 18, no. 2, pp. 735–742, 2016.

[28] T. S. van der Poll, J. A. Love, T.-Q. Nguyen, and G. C. Bazan, "Non-basic high-performance molecules for solution-processed organic solar cells," *Adv. Mater.*, vol. 24, no. 27, pp. 3646–3649, Jul. 2012.

[29] S. H. Mohamed, F. M. El-Hossary, G. A. Gamal, and M. M. Kahlid, "Properties of indium tin oxide thin films deposited on polymer substrates," *Acta Phys. Polonica A*, vol. 115, no. 3, pp. 704–708, Mar. 2009.

[30] J. Shi *et al.*, "Designing high performance all-small-molecule solar cells with non-fullerene acceptors: comprehensive studies on photoexcitation dynamics and charge separation kinetics," *Energy Environ. Sci.*, vol. 11, no. 1, pp. 211–220, 2018.
[31] X. Xu *et al.*, "Influence of gold-silica nanoparticles on the performance of small-molecule bulk heterojunction solar cells," *Org. Electron.*, vol. 22, pp. 20–28, Jul. 2015.
[32] P. Vincent *et al.*, "Indoor-type photovoltaics with organic solar cells through optimal design," *Dyes Pigments*, vol. 159, pp. 306–313, Dec. 2018.
[33] Y. Long *et al.*, "Effect of annealing on exciton diffusion in a high performance small molecule organic photovoltaic material," *ACS Appl. Mater. Interfaces*, vol. 9, no. 17, pp. 14945–14952, 2017.
[34] J. Miao, H. Chen, F. Liu, B. Zhao, L. Hu, Z. He, and H. Wu, "Efficiency enhancement in solution-processed organic small molecule: Fullerene solar cells via solvent vapor annealing," *Appl. Phys. Lett.*, vol. 106, no. 18, 2015, Art. no. 183302.
[35] F. Zhang *et al.*, "Influence of PC60BM or PC70BM as electron acceptor on the performance of polymer solar cells," *Solar Energy Mater. Solar Cells*, vol. 97, pp. 71–77, Feb. 2012.
[36] N. Sharma, S. K. Gupta, and C. M. S. Negi, "Influence of active layer thickness on photovoltaic performance of PTB7:PC70BM bulk heterojunction solar cell," *Superlattices Microstruct.*, vol. 135, Nov. 2019, Art. no. 106278.
[37] A. Ray, A. Bauri, and S. Bhattacharya, "Absorption spectrophotometric, fluorescence and quantum chemical investigations on non-covalent interaction between PC70BM and designed diporphyrin in solution," *Spectrochim. Acta Part A Mol. Biomol. Spectrosc.*, vol. 134, pp. 566–573, Jan. 2015.
[38] S. Günes, H. Neugebauer, and N. S. Sariciftci, "Conjugated polymer-based organic solar cells," *Chem. Rev.*, vol. 107, no. 4, pp. 1324–1338, Apr. 2007.
[39] J. A. Love *et al.*, "Film morphology of high efficiency solution-processed small-molecule solar cells," *Adv. Funct. Mater.*, vol. 23, no. 40, pp. 5019–5026, Oct. 2013.
[40] Z. Zhang, Z. Ding, X. Long, C. Dou, J. Liu, and L. Wang, "Organic solar cells based on a polymer acceptor and a small molecule donor with a high open-circuit voltage," *J. Mater. Chem. C*, vol. 5, no. 27, pp. 6812–6819, 2017.
[41] C. J. Takacs *et al.*, "Mapping orientational order in a bulk heterojunction solar cell with polarization-dependent photoconductive atomic force microscopy," *ACS Nano*, vol. 8, no. 8, pp. 8141–8151, 2014.
[42] J. A. Love *et al.*, "Interplay of solvent additive concentration and active layer thickness on the performance of small molecule solar cells," *Adv. Mater.*, vol. 26, no. 43, pp. 7308–7316, 2014.
[43] S. Engmann *et al.*, "Reduced bimolecular recombination in blade-coated, high-efficiency, small-molecule solar cells," *J. Mater. Chem. A*, vol. 5, no. 15, pp. 6893–6904, 2017.
[44] J. G. Sánchez *et al.*, "Impact of inkjet printed ZnO electron transport layer on the characteristics of polymer solar cells," *RSC Adv.*, vol. 8, no. 24, pp. 13094–13102, 2018.
[45] L. Lu, W. Chen, T. Xu, and L. Yu, "High-performance ternary blend polymer solar cells involving both energy transfer and hole relay processes," *Nat. Commun.*, vol. 6, p. 7327, Jun. 2015.
[46] L. K. Jagadamma, M. T. Sajjad, V. Savikhin, M. F. Toney, and I. D. W. Samuel, "Correlating photovoltaic properties of a PTB7-Th:PC71BM blend to photophysics and microstructure as a function of thermal annealing," *J. Mater. Chem. A*, vol. 5, no. 28, pp. 14646–14657, 2017.
[47] S. R. Cowan, A. Roy, and A. J. Heeger, "Recombination in polymer-fullerene bulk heterojunction solar cells," *Phys. Rev. B, Condens. Matter*, vol. 82, no. 24, Dec. 2010, Art. no. 245207.
[48] S. R. Cowan, W. L. Leong, N. Banerji, G. Dennler, and A. J. Heeger, "Identifying a Threshold Impurity Level for Organic Solar Cells: Enhanced First-Order Recombination Via Well-Defined PC84BM Traps in Organic Bulk Heterojunction Solar Cells," *Adv. Funct. Mater.*, vol. 21, no. 16, pp. 3083–3092, Aug. 2011.
[49] J. Zhao *et al.*, "High-efficiency non-fullerene organic solar cells enabled by a difluorobenzothiadiazole-based donor polymer combined with a properly matched small molecule acceptor," *Energy Environ. Sci.*, vol. 8, no. 2, pp. 520–525, 2015.
[50] E. Osorio *et al.*, "Degradation analysis of encapsulated and nonencapsulated TiO_2/PTB7:$PC_{70}BM$/V_2O_5 solar cells under ambient conditions via impedance spectroscopy," *ACS Omega*, vol. 2, no. 7, pp. 3091–3097, 2017.
[51] Z. Peng *et al.*, "One-step coating inverted polymer solar cells using a conjugated polymer as an electron extraction additive," *J. Mater. Chem. A*, vol. 3, no. 41, pp. 20500–20507, 2015.
[52] D. Rathee, S. K. Arya, and M. Kumar, "Capacitance-voltage analysis of a high-k dielectric on silicon," *J. Semicond.*, vol. 33, no. 2, 2012, Art. no. 22001.
[53] B. Arredondo, B. Romero, G. D. Pozo, M. Sessler, C. Veit, and U. Würfel, "Impedance spectroscopy analysis of small molecule solution processed organic solar cell," *Solar Energy Mater. Solar Cells*, vol. 128, pp. 351–356, Sep. 2014.
[54] S. Thiagarajan, M. Thaiyan, and R. Ganesan, "Physical property exploration of highly oriented V_2O_5 thin films prepared by electron beam evaporation," *New J. Chem.*, vol. 39, no. 12, pp. 9471–9479, 2015.
[55] G. Garcia-Belmonte, A. Munar, E. M. Barea, J. Bisquert, I. Ugarte, and R. Pacios, "Charge carrier mobility and lifetime of organic bulk heterojunctions analyzed by impedance spectroscopy," *Org. Electron.*, vol. 9, no. 5, pp. 847–851, 2008.
[56] A. S. Grove, "*p-n* Junctions," in *Physics and Technology of Semiconductor Devices*. New York, NY, USA: Wiley, 1967, pp. 169–172.